

# The large scale structure of the soft X-ray background

## III. Cosmological implications

A.M. Soltan<sup>1</sup>, M. Freyberg<sup>2</sup>, G. Hasinger<sup>3</sup>, T. Miyaji<sup>2</sup>, M. Treyer<sup>4</sup>, and J. Trümper<sup>2</sup>

<sup>1</sup> Nicolaus Copernicus Astronomical Center, Bartycka 18, PL-00-716 Warsaw, Poland

<sup>2</sup> Max-Planck-Institut für Extraterrestrische Physik, Giessenbachstrasse, D-85748 Garching, Germany

<sup>3</sup> Astrophysikalisches Institut Potsdam, An der Sternwarte 16, D-14482 Potsdam, Germany

<sup>4</sup> Laboratoire d'Astronomie Spatiale, Marseille, France

Received 8 April 1999 / Accepted 13 July 1999

**Abstract.** The auto-correlation function of the X-ray background in the range of angular scales  $0.3\text{--}20^\circ$  is determined using the *ROSAT* All-Sky Survey. In the power-law approximation, our best fit estimate is  $w(\theta) = (0.0058/\theta)^{1.1}$ . At the small separation end, this is substantially above previous estimates based on *ROSAT* pointings. The present upward revision of the correlation amplitude results from variations in the background intensity at angular scales larger than the field of view of the X-ray telescope.

Various assumptions for the local clustering amplitude, clustering evolution rate and luminosity/density evolution of the sources producing the background are explored, and the predicted auto-correlation functions compared with the measured fluctuations. We show that the large amplitude of the background angular auto-correlation function is incompatible with the weak clustering amplitude observed for normal galaxies, while it is marginally compatible with some measurements of the AGN clustering amplitude at moderate redshifts.

**Key words:** cosmology: observations – cosmology: large-scale structure of Universe – X-rays: general

### 1. Introduction

The potential role of the X-ray background (XRB) for the investigation of large scale structures in the Universe has been recognized in recent years and explored in various ways (e.g. Carrera et al. 1997, Barcons et al. 1998, Boughn 1998, Treyer et al. 1998). The total background at and below  $\sim 1$  keV is a mixture of extragalactic radiation and diffuse hot plasma emission unevenly distributed in the Galaxy (Hasinger 1992). Away from the main regions of galactic contamination however, a large fraction of the soft XRB is now resolved into weak extragalactic sources. According to Hasinger et al. (1998), 70–80 % of the XRB is produced by  $\sim 10^3$  sources per sq.deg. It is likely that the remaining fraction also originates in still fainter

discrete sources. It is expected that some of these sources are associated with clusters of galaxies. Thus, some portion of the XRB is produced by the extended sources. AGNs (quasars and Seyfert galaxies) constitute roughly 80 % of the sources above the *ROSAT* Deep Survey limit (Schmidt et al. 1998). The redshift distribution of the extragalactic objects in the Schmidt et al. sample is roughly flat between  $z \sim 0.2$  and  $\sim 2$  with a tail extending to  $z \sim 3$ . Although the redshift distribution of the XRB flux itself (i.e. the integrated flux per redshift bin) is not well constrained by observations, it appears that a substantial fraction of the XRB comes from objects spread over a wide range of redshifts. The variations of the background flux on the celestial sphere depend on the spatial clustering and on the luminosity density of these sources at all redshift. Thus measuring the XRB fluctuations allows us to study the clustering properties of high redshift sources (although in a diluted form due to the integration along the line of sight).

In turn, understanding the evolution of source clustering as a function of redshift allows us to study galaxy formation. In theoretical considerations (e.g. Matarrese et al. 1997, Moscardini et al. 1998, Peacock 1998), galaxies are identified to the peaks of the density fluctuations whose growth is driven by gravitational instability in the non-linear regime. Within this framework, galaxy clustering does not imitate that of the dark matter. The so-called bias factor which relates the amplitudes of the respective auto-correlation functions seems to increase with redshift (e.g. Bagla 1998, Moscardini et al. 1998), but this question is still very much under investigation (e.g. Tegmark & Peebles 1998). Information on the large scale distribution of X-ray sources complemented by optical surveys of high redshift galaxies and quasars are crucial to measure the bias variations and - eventually - to understand the formation of structures in the Universe.

In this paper we measure the XRB fluctuations from the *ROSAT* All-Sky Survey (RASS) and try to evaluate the clustering properties of the XRB sources by examining a range of models for their flux distribution and spatial clustering. The auto-correlation function (ACF) is determined in the next section. This new estimate of the XRB ACF is comparable to that

Send offprint requests to: A.M. Soltan

Correspondence to: soltan@camk.edu.pl

of Softan et al. (1996, hereafter S96) but differs substantially from earlier estimates derived from *ROSAT* pointing observations by Softan & Hasinger (1994). In Sect. 2.2 and in the Appendix we discuss this discrepancy and show that the lack of data on large scale fluctuations in the pointing observations substantially lowered the ACF estimates of Softan & Hasinger (1994). The relationship between the spatial and the angular correlation functions as well as the effects of cosmic evolution in the source luminosity function are discussed in Sect. 3. In Sect. 4, a range of models describing the evolution of the source luminosity function and clustering properties are investigated, and the predicted ACFs compared with the observed fluctuations. We discuss our results in Sect. 5 and comment on the possible effects of nearby groups of galaxies on the ACF.

## 2. The auto-correlation function of the XRB

We quantify the angular fluctuations of the XRB intensity by means of its angular auto-correlation function (ACF):

$$w(\theta) = \frac{\langle I(\mathbf{n})I(\mathbf{n}') \rangle}{\langle I \rangle^2} - 1, \quad (1)$$

where  $I(\mathbf{n})$  is the intensity of the XRB in the direction  $\mathbf{n}$ ,  $I(\mathbf{n})I(\mathbf{n}')$  is a product of intensities with angular separation  $\theta$ , and  $\langle \dots \rangle$  denotes the expectation values of the corresponding quantities. In X-ray astronomy, the radiation distribution is typically represented by an array of count rates per pixel. As an estimator of the ACF, the expectation values are replaced by the corresponding average quantities calculated from the available data:

$$W(\theta) = \frac{\overline{I_i I_{j|\theta}}}{\overline{I}^2} - 1, \quad (2)$$

where  $I_i$  is the count rate in the  $i$ -th pixel and the overlines denote the sample average.

### 2.1. Observational data and results at large angular scales

The elaborate procedures used in constructing the X-ray maps are described by Snowden et al. (1992, 1994), Snowden & Freyberg (1993) and Plucinsky et al. (1993). The maps and their production itself are shown in Snowden et al. (1995, 1997) for 40' and 12' spatial resolution, respectively. In the following analysis we use the 12' resolution maps where point sources have not been removed but non-cosmic (diffuse!) background (i.e. solar system and internal) contributions have been carefully modeled and subtracted (see Snowden et al., 1997, and references therein). This is especially important for studies of diffuse emission and autocorrelation analyses as residual contaminations present in the maps would diminish the ACF signal. Visual inspection of these maps (S96) shows that the fine features of the extragalactic component are outshined by the emission of hot galactic plasma over a large portion of the sky. In the present investigation we use a region of the northern galactic hemisphere ( $70^\circ < l < 250^\circ$  and  $b > 40^\circ$ , approximately 1 steradian) which seems minimally contaminated by

local emission (S96). We use the same method as S96 to isolate the ACF of the extragalactic component from the local contamination.

We utilize RASS maps in two energy bands: R5 and R6 centered at 0.83 and 1.15 keV, respectively (Snowden et al. 1994). The R6 band least affected by any non-cosmic contamination while the R5 band suffers occasionally from oxygen  $K\alpha$  fluorescent line emission due to scattered solar X-rays (SSX). Though this component has been subtracted, there is an increased uncertainty in the diffuse emission due to the high number of counts in the SSX component. Since the galactic component is significantly softer than the extragalactic one, it is possible to split the total fluctuations into local and extragalactic components described by two independent ACF's. Let  $n^s$  and  $n^h$  denote the total count rates in the R5 (*soft*) and R6 (*hard*) energy channels respectively. Photons of galactic “ $g$ ” and extragalactic “ $e$ ” origin contribute to these two energy bands in different proportions:

$$\begin{aligned} n^s &= n_g^s + n_e^s \\ n^h &= n_g^h + n_e^h. \end{aligned} \quad (3)$$

The relative contributions of both (local and extragalactic) components to each energy band depend on their spectral characteristics and is described by their “softness” ratios:

$$\begin{aligned} r_g &= n_g^s / n_g^h \\ r_e &= n_e^s / n_e^h. \end{aligned} \quad (4)$$

In S96  $r_g$  and  $r_e$  are estimated at 5.0 and 0.66, respectively. Accordingly, in the R6 band the mean galactic contribution,  $\overline{n_g^h}$ , amounts to only  $\sim 3\%$  of the total count rate,  $\overline{n^h}$ , while it reaches 22% in the softer (R5) band.

The ACFs of the galactic and extragalactic component in the RASS maps,  $w_g(\theta)$  and  $w_e(\theta)$ , are related to the ACFs of the total counts in both bands,  $w^h(\theta)$  and  $w^s(\theta)$  (we omit overlines for clarity) in the following way:

$$\begin{aligned} (n_e^h)^2 w_e(\theta) + (n_g^h)^2 w_g(\theta) &= (n^h)^2 w^h(\theta) \\ (n_e^s)^2 w_e(\theta) + (n_g^s)^2 w_g(\theta) &= (n^s)^2 w^s(\theta). \end{aligned} \quad (5)$$

Fig. 1a shows the ACFs of the total counts in bands R5 and R6. Note the larger scatter here in both bands than in Fig. 2a of S96. This results from a slightly different treatment of the data. In S96 our main objective was to investigate the weak correlation signal between the count rates and rich clusters of galaxies at separations larger than  $\sim 2^\circ$ . In order to minimize the statistical noise in the X-ray data, we had imposed a threshold for the maximum count rates approximately  $3\sigma$  above the mean. This cut-off significantly reduced the scatter but also slightly diminished the amplitude of the ACF.

The ACFs of the galactic and extragalactic components are shown in Fig. 1b. Note that each ACF describes the relative fluctuations of the respective components. Despite the large ACF amplitude of the local component, the total XRB fluctuations in the R6 band are still dominated by the extragalactic signal because the local counts only represent a small fraction of the total flux. Consequently, the discrepancy between the ACF of the raw

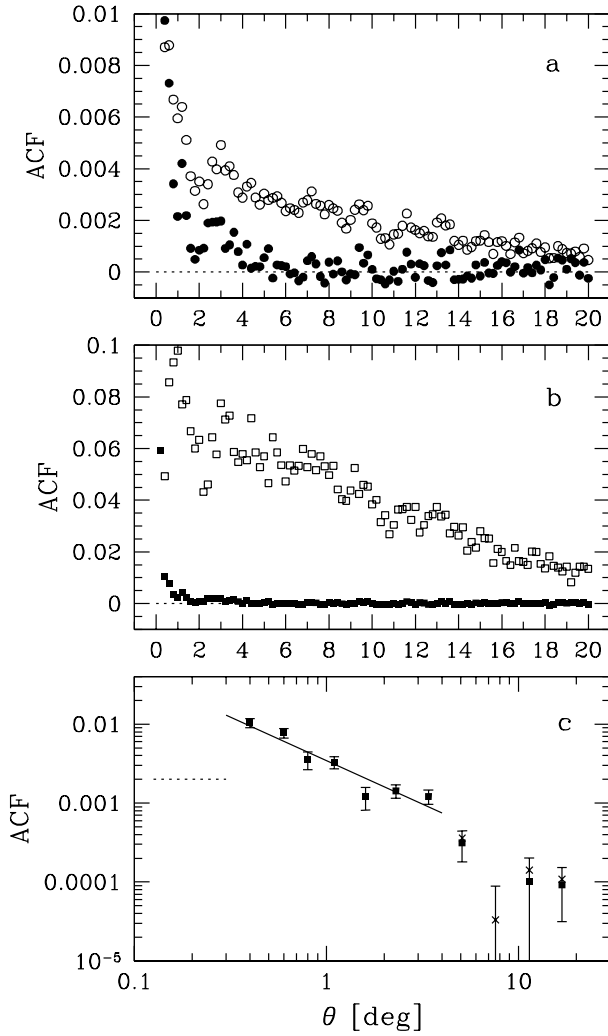


**Fig. 1.** **a** The ACFs of the raw count rates in the energy band R5 - open circles, and R6 - filled circles, **b** The ACF of the galactic count rate distribution - open squares, and extragalactic - filled squares; **c** The ACF of the extragalactic component - squares, the ACF of the raw R6 count rates - crosses; note the logarithmic scale at both axes.

counts in the R6 band and that of the extragalactic component (Fig. 1c) is small and only noticeable at separations larger than  $\sim 3^\circ$ .

The error bars represent  $1\sigma$  uncertainties resulting from pixel to pixel fluctuations in the count rates. Over the whole range of separations the ACF slope is slightly steeper than the „canonical” value of  $\gamma = -0.8$ . At separations smaller than  $4^\circ$  the least square fit gives  $\gamma = -1.1 \pm 0.2$ , where the uncertainty is calculated using the measured deviations from the best fit shown by the solid line in Fig. 1c:

$$w(\theta) = (\theta/\theta_0)^{-1.1}, \quad (6)$$

with  $\theta_0 = (5.8^{+0.7}_{-0.6}) \times 10^{-3}$ . A similar slope of  $-1.1$  was found by Cress et al. (1996) for the ACF of radio sources brighter than  $3$  mJy in the FIRST radio survey. Most of these sources are related to various classes of AGN and are distributed at cosmological distances. Thus, both surveys probe similar and proba-

bly partially overlapping samples of objects and one may expect comparable slopes of the corresponding correlation functions.

As the size of the area used in the analysis is much larger than the maximum separation at which the ACF signal is detectable, the data satisfy the *fair sample* requirement and the ACF thus constitutes a representative estimate of the XRB fluctuations. One should also note that the measured range of ACF amplitudes covers almost two orders of magnitude. This implies that potential fluctuations at still larger scales, i.e. at  $\theta > 20^\circ$ , should not affect the present estimate. At separations greater than  $\sim 6^\circ$  however, the signal-to-noise ratio drops below 2 and therefore the present calculations only provide an upper limit to the ACF at these separations.

## 2.2. Small angular scales

The RASS data binned in  $12' \times 12'$  pixels can be used to measure the ACF at separations greater than  $\sim 0.3^\circ$ . However, the monotonic slope of the ACF over a wide range of separations (Fig. 1c) suggests that we may reasonably extrapolate it to the smaller separations covered by the *ROSAT* PSPC pointings. Using a number of these pointing observations, Soltan & Hasinger (1994) derived an upper limit to the ACF at separations between  $\sim 2'$  and  $\sim 20'$ , shown by the dotted line in Fig. 1c. The strong signal of the RASS data extrapolated to these small angular separations substantially exceeds the upper limit derived from pointings. This discrepancy can be explained in the light of the present measurement: the pointing estimates only describe fluctuations on scales smaller than the field of view. The large scale variations which the present measurement reveal and which strongly affect the intensity averaged over the individual pointings, are effectively removed from the pointing calculation, hence a severe underestimate of the ACF amplitude in this case. A detailed discussion of this question is given in the Appendix, where we show that after proper adjustment, the pointing estimates can be reconciled with the RASS results. One should note also that the ACF estimate based on pointings was calculated *after* removal of the discrete sources, what additionally reduced the ACF signal. The magnitude of this effect will be discussed in our next paper.

## 3. Spatial vs. angular fluctuations of the XRB

We assume that the fluctuations in the XRB flux are generated entirely by a non uniform distribution of discrete sources. The redshift distribution of known X-ray sources is very wide. Consequently, interpreting the angular fluctuations is not straightforward and requires data on the statistical properties of the sources as a function of redshift.

The total XRB flux density  $I(E)$  at energy  $E$ , is the integrated emission from consecutive redshift shells:

$$I(E) = \int_{z_{\min}}^{z_{\max}} dz \frac{dI(z, E)}{dz}, \quad (7)$$

where:

$$\frac{dI(z, E)}{dz} = \frac{dV}{dz} F(z, E), \quad (8)$$

$$\frac{dV}{dz} = \omega \frac{c}{H_0} \frac{D_L^2}{(1+z)^3} \frac{1}{\sqrt{1+2q_0z}} \quad (9)$$

is the co-moving volume at redshift  $z$  within a solid angle  $\omega$ ,  $D_L$  is the luminosity distance ( $c$  - velocity of light,  $H_0$  - Hubble constant, and  $q_0$  - deceleration parameter), and:

$$F(z, E) = \frac{\mathcal{L}_z[E(1+z)](1+z)}{4\pi D_L^2} \quad (10)$$

is the flux density observed at energy  $E$  produced by sources within a volume of  $1 \text{ Mpc}^3$  (co-moving) at redshift  $z$ ;  $\mathcal{L}_z(E)$  is the luminosity density at redshift  $z$ .

According to Eq. (1), the angular ACF of the XRB is given by

$$w(\theta) = \frac{1}{I(E)^2} \int_{z_{\min}}^{z_{\max}} dz' \frac{dV}{dz'} \int_{z_{\min}}^{z_{\max}} dz \frac{dV}{dz} \langle F(z, E) F'(z', E) \rangle - 1, \quad (11)$$

where the angular separation between the volume elements producing  $F$  and  $F'$  is equal to  $\theta$ . One can express the ensemble average of the flux product  $\langle F(z, E) F'(z', E) \rangle$  by the corresponding product of luminosity densities which is related to the spatial correlation function of X-ray luminosities,  $\xi_{\mathcal{L}}[r, z]$ :

$$\langle \mathcal{L}_z \mathcal{L}_{z'} \rangle = \mathcal{L}_z^2 (1 + \xi_{\mathcal{L}}[r, z]), \quad (12)$$

where  $r$  is the distance between two points at redshift  $z$  and  $z'$  respectively separated by an angle  $\theta$ . In the equation above it is explicitly assumed that  $\xi_{\mathcal{L}}[r, z] \neq 0$  for separations much smaller than the characteristic scale of variations of  $\mathcal{L}_z$ . Using standard approximations, Eqs. (11) and (12) combined give the *Limber equation* (Limber 1953):

$$w(\theta) = \left( \frac{A}{I(E)} \right)^2 \int_{z_{\min}}^{z_{\max}} dz \frac{dV}{dz} (1+z)^{-4} (1+2q_0z)^{-1} (\mathcal{L}_z[E(1+z)])^2 \int dz' \xi_{\mathcal{L}}[r(z, z', \theta), z], \quad (13)$$

where  $A = \frac{\omega c}{4\pi H_0}$ . The second integration covers the range where  $\xi_{\mathcal{L}} \neq 0$ . In the rest of the paper we use a standard Friedman cosmological model with  $H_0 = 100 \text{ km s}^{-1} \text{ Mpc}^{-1}$  and  $q_0 = 0.5$  (all data quoted from the literature are scaled assuming these parameters). Unless stated otherwise, X-ray fluxes and luminosities refer to the energy range 0.5 - 2 keV.

### 3.1. Evolution of luminosity density

The X-ray source population creating the XRB is nonhomogeneous. The largest contribution comes from AGNs, predominantly QSOs and Seyfert galaxies (Hasinger 1998). A non negligible fraction of the XRB is also due to „normal” galaxies and clusters of galaxies. Although data on the rate of evolution of galaxies and clusters are scarce, these objects exhibit at most weak evolutionary effects, while it is well established that quasars are subject to strong evolution. For the purpose of the present analysis, we simply divide X-ray sources into two

groups: (a) evolving sources with a quasar-like rate of evolution, and (b) nonevolving sources representing galaxies and clusters. The relative local contribution of both components is not well determined observationally. Because of the trivial constraint that the total contribution from nonevolving and evolving sources integrated over redshift must amount to the observed intensity of the XRB, the local contribution of the evolving population is defined by its rate of evolution (see below).

The systematic variations of  $\mathcal{L}_z$  caused by the red-shift between the emitted and observed energies (the  $K$ -correction) depend on the spectral energy distribution of the XRB sources. The distribution of spectral indices in the considered energy range is wide because of the variety of emission mechanisms and, perhaps more importantly, because of the wide range of column densities of cold gas absorbing soft photons at the sources. In the calculations below we use a single energy index of  $-1$  for both evolving and nonevolving sources. Thus,  $\mathcal{L}_z[E(1+z)] = \mathcal{L}_z[E](1+z)^{-1}$ . As cosmic (luminosity/density) evolution effects strongly dominate the global redshift variations of the light density (see below), this simple  $K$ -correction model does not significantly affect our conclusions.

As mentioned earlier, the AGN X-ray luminosity function is subject to strong cosmological evolution. Using a combination of the *Einstein* Medium Sensitivity Survey (EMSS) and 5 deep *ROSAT* PSPC exposures, Boyle et al. (1994) considered several evolution models. They found that a *luminosity evolution* (LE) of the form  $L_X \sim (1+z)^k$  with  $k = 3.25$  for  $z \leq 1.6$  and constant comoving space density at higher redshifts satisfactorily described the observations. However, the analysis by Miyaji et al. (1998b) from a combination of various *ROSAT* surveys ranging from the shallow *ROSAT* All-Sky Survey to the Ultra-Deep Survey reaching a flux limit of  $\approx 2 \times 10^{-15} \text{ erg s}^{-1} \text{ cm}^{-2}$ , a pure luminosity evolution model is practically ruled out, in favor of a *luminosity dependent density evolution* (LDDE).

In the LDDE model, the density evolution rate is high for luminous AGNs and drops at lower luminosities. The Miyaji et al. model specifies the shape and redshift variation of the soft X-ray luminosity function; in particular, it predicts that the number of objects increases up to redshift  $\sim 1.5$  and remains stable at higher redshifts.

These evolutionary effects introduce a strong redshift dependence in the light density integral:

$$\mathcal{L}_z = \int L_X \Phi_z(L_X) dL_X. \quad (14)$$

Denoting the luminosity density of nonevolving sources by  $\mathcal{L}^n$  and the local luminosity density of evolving sources by  $\mathcal{L}_o^e$ , we have:

$$\mathcal{L}_z = \mathcal{L}^n + \mathcal{L}_o^e \cdot \mathcal{E}(z), \quad (15)$$

where  $\mathcal{E}(z)$  is the evolution rate. Introducing  $f = \mathcal{L}_o^e / \mathcal{L}^n$ , the ratio of the local light densities from evolving and nonevolving sources respectively, Eq. (15) takes the form:

$$\mathcal{L}_z = \mathcal{L}_o \frac{1 + f\mathcal{E}(z)}{1 + f}. \quad (16)$$

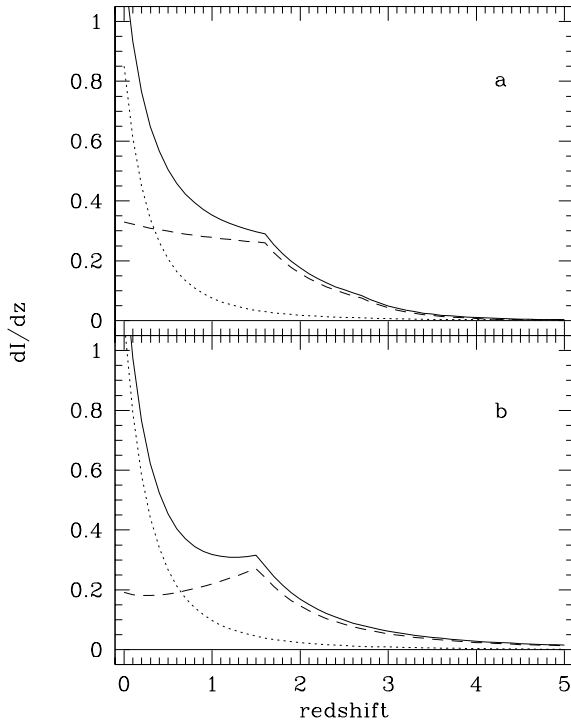


**Fig. 2a and b.** Redshift distribution of the XRB for two evolutionary scenarios: **a** based on the Boyle et al. (1994) pure luminosity evolution model,  $\mathcal{E} \sim (1+z)^{3.25}$  for  $z < 1.6$ , and  $\mathcal{E} = \text{const.}$  at  $1.6 < z < 2.7$ , **b** Miyaji et al. (1998b) model of luminosity dependent density evolution. Dashed lines - evolving objects, dotted lines - nonevolving objects, solid lines - total contribution. See the text for details.

Sołtan et al. (1997) estimate of the X-ray luminosity spatially correlated with optical light is  $\mathcal{L}_o \sim 9 \times 10^{38} \text{ erg s}^{-1} \text{ Mpc}^{-3}$ , comparable to the result of Treyer & Lahav (1996).

For  $f = 0$  (no evolving population), the local (non evolving) population integrated over redshift produces roughly  $\sim 30\%$  of the XRB. To determine  $f$  in the Boyle et al. model (LE), we assume that the total luminosity density from both components at  $z = 0$  amounts to the above value of  $\mathcal{L}_o$  (Sołtan et al. 1997), and that the total flux from both populations integrated over redshift amounts to the total observed intensity of the XRB. This yields:  $f = 0.60$  (i.e. the local light density of the evolving sources is 60% that of the nonevolving sources).

We determine  $f$  differently for the Miyaji et al. model (LDDE). The local light density from the evolving population can be computed directly from the X-ray luminosity function:  $\mathcal{L}_o^e \sim 2.1 \times 10^{38} \text{ erg s}^{-1} \text{ Mpc}^{-3}$ . These sources produce approximately 56% of the total XRB. To obtain the remaining fraction from the nonevolving objects requires  $\mathcal{L}^n \approx 1.2 \times 10^{39} \text{ erg s}^{-1} \text{ Mpc}^{-3}$ . The resulting local luminosity density from both populations is therefore:  $\mathcal{L}_o \approx 1.4 \times 10^{39} \text{ erg s}^{-1} \text{ Mpc}^{-3}$ . This value is a factor of  $\sim 1.6$  larger than the Sołtan et al. estimate, which we consider an acceptable deviation given the uncertainties involved in both investigations. This model yields  $f = 0.39$ .

Fig. 2 shows the redshift distribution of the XRB flux,  $dI/dz$  (Eq. 8) for the two evolution models described above (LE and

LDDE). (The distributions are normalized to the total background.) Both models look quite similar despite the different assumptions involved. In particular, both distributions spread over a very wide range of redshift. This effectively dilutes the fluctuations integrated over redshift and therefore the observed angular auto-correlation signal is expected to be much reduced compared to the average amplitude of the spatial variations.

### 3.2. Evolution of the spatial correlation function

The spatial correlation function  $\xi_{\mathcal{L}}$  defined in Eq. (13) is the 2-point correlation function of the luminosity density distribution. This distribution may be different from the spatial distribution of the sources themselves. To account for this distinction, one should introduce a luminosity-source bias factor,  $b_{\mathcal{L}}(z)$ <sup>1</sup>, relating the correlation functions of both distributions:

$$\xi_{\mathcal{L}} = b_{\mathcal{L}}^2(z) \xi \quad (17)$$

where  $\xi$  is the 3D ACF of the source distribution. Reliable estimates on  $b_{\mathcal{L}}(z)$  are not available, and we assume  $b_{\mathcal{L}}(z) \equiv 1$ . Considering the various uncertainties already involved in our models, we believe that this assumption is not critical for the present calculations.

The clustering properties of different classes of objects are widely discussed in the literature. We assume that the spatial distribution of the nonevolving sources resembles that of the general galaxy population. The 3D ACF of galaxies at separations smaller than  $\sim 10\text{--}20$  Mpc has a well defined power law shape  $\xi = (r/r_o)^{-\gamma}$  with a slope  $\gamma \approx 1.8$  and a correlation length  $r_o \approx 5$  Mpc (e.g. Groth & Peebles 1977, Ratcliffe et al. 1998, and references therein). At larger separations the ACF measurements are subject to increasing uncertainties; it is generally accepted that the function turns over above  $\sim 20$  Mpc, but there are significant differences among various investigations.

Observational evidences of clustering evolution are usually expressed in the following form (e.g. Moscardini et al. 1998):

$$\xi[r, z] = \xi[r/(1+z), 0] (1+z)^{-(3+\epsilon)}, \quad (18)$$

where  $r$  denotes the comoving separation and all the evolutionary effects are contained in the scaling factor  $(1+z)^{-\epsilon}$ . For the standard power-law model  $\xi[r, 0] = (r/r_o)^{-\gamma}$  Eq. 18 becomes:

$$\xi[r, z] = \xi[r, 0] (1+z)^{-(3-\gamma+\epsilon)}. \quad (19)$$

Several studies of faint galaxy clustering seem to favour an increase of the clustering amplitude with time at a rate comparable to the linear growth of fluctuations due to gravitational instability (although this correspondence seems to be accidental (Moscardini et al. 1998)). According to most investigations:  $\epsilon \approx 1 \pm 1$  (e.g. Shepherd et al. 1997, Woods & Fahlman 1997, Roche & Eales 1998), albeit it is likely that the parameterization used in Eq. 18 does not provide a good fit to the data

<sup>1</sup> Note that various definitions of bias factor specific to concrete problems are used in the literature, and that the present definition of  $b_{\mathcal{L}}(z)$  is different than the bias factor relating the distribution of galaxies to the mass density fluctuations.

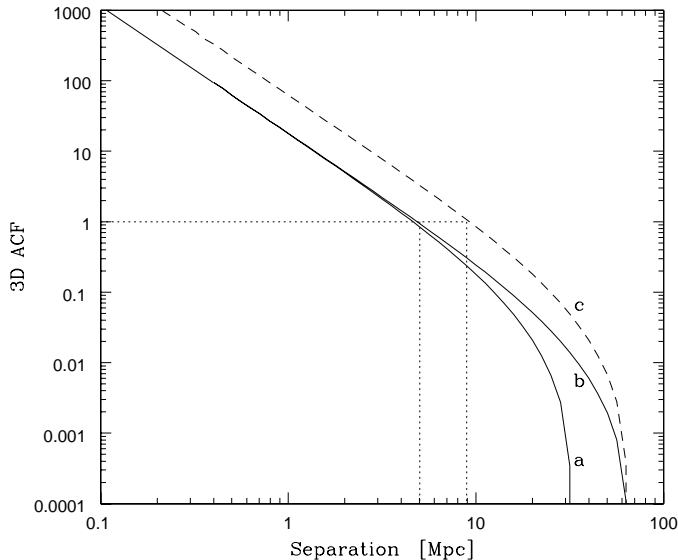


**Fig. 3.** Model 3D ACF used in the calculations. Solid curves (*a* and *b*) represent the ACF with low correlation length  $r_o \approx 5$  Mpc, usually ascribed to ‘normal’ galaxies; dashed curve (*c*) with higher normalization of  $r_o = 9$  Mpc is a model ACF for AGN. Dotted lines show the respective correlation lengths. See the text for details.

(Connolly et al. 1998). Fig. 2 shows that the contribution of the nonevolving objects to the XRB decreases rapidly with redshift, therefore the rate of clustering evolution only weakly affects the present calculations.

Studies of AGN clustering and clustering evolution provide results which are difficult to reconcile. Andreani & Cristiani (1992) found that QSOs were more strongly clustered than galaxies, with a characteristic clustering length of  $r_o \sim 10$  Mpc roughly constant in comoving coordinates. Extensive studies of Seyfert galaxies extracted from the IRAS all-sky survey and several QSO samples selected using optical or UV criteria (Shanks & Boyle 1994, Georantopoulos & Shanks 1994, Croom & Shanks 1996) confirmed that AGNs do not exhibit strong clustering evolution in comoving coordinates, but that at low redshift the AGN clustering amplitude is consistent with that of normal galaxies ( $r_o \approx 6$  Mpc). More recently, Carrera et al. (1998) argue that both the local clustering amplitude and the clustering evolution of AGNs are similar to that of ‘normal’ galaxies. Carrera et al.’s result is of special importance for the present investigation because it is based solely on X-ray selected AGNs, while all the previous results were based on samples selected at other wavelengths. Stable clustering in *comoving* coordinates corresponds to  $\epsilon \approx -1.2$ . Stronger clustering evolution, with  $\epsilon \approx -2.5$ , has also been reported (La Franca et al. 1998). The measurements of the AGN ACF slope are also subject to large uncertainties, but consistent with  $\gamma \approx 1.8$ , as measured for galaxies.

We try to assess the effects of clustering amplitude and evolution on the XRB fluctuations by examining various combinations of clustering models. Three different local 3D ACFs are used in the calculations (models *a*, *b* and *c*, shown in Fig. 3). At small separations, all three functions are power-laws with a

**Table 1.** AGN luminosity and clustering models

Model	Luminosity evolution <sup>1</sup>	$\epsilon$	3D ACF <sup>2</sup>	Clustering evolution type <sup>3</sup>
A	LE	0.8	a	v
B	LDDE	0.8	a	v
C	LDDE	-1.2	c	v
D	LE	-1.2	c	v
E	LDDE	-2.5	b	v
F	LDDE	-2.5	b	h
G	LDDE	-2.5	c	h
H	LE	-2.5	c	h

<sup>1</sup> LE – luminosity evolution model, LDDE – luminosity dependent density evolution model,

<sup>2</sup> Notation as in Fig. 3,

<sup>3</sup> Clustering evolution according to Eq. 19 – v (‘vertical’), and Eq. 20 – h (‘horizontal’).

‘standard’ slope of  $-1.8$ . The observational constraints become weak at separations larger than  $\sim 20$  Mpc. We consider two ‘cutoff lengths’: in model *a* the correlation function extends to  $\sim 30$  Mpc, while in models *b* and *c* it extends to  $\sim 60$  Mpc. Models *a* and *b* are identical at small separations and in both cases  $\xi = 1$  at  $\sim 4.5$ – $5$  Mpc. Model *c* has a higher normalization, with  $\xi = 1$  at  $9$  Mpc.

The clustering evolution law defined in Eq. 19 only allows for variations in the ACF normalization (a ‘vertical’ shift). To allow for possible variations in the cutoff length, we also consider a ‘horizontal’ shift:

$$\xi[r, z] = \xi[r(1+z)^{\frac{3-\gamma+\epsilon}{\gamma}}, 0]. \quad (20)$$

At low separations (in the power-law regime of the ACF), both evolution laws (Eqs. 19 and 20) are equivalent. Differences arise above the cutoff length where the ACF slope drops exponentially. However simple, Eqs. 19 and 20 qualitatively reproduce the basic evolution patterns predicted by various numerical simulations (e.g. Matarrese et al. 1997).

#### 4. Models of the XRB fluctuations

Various combinations of evolution models for both the luminosity density and the clustering properties are inserted into Eq. 13. A representative selection of models is listed in Table 1. The resulting angular correlation functions are compared with the observed one (Fig. 4).

Because the contribution of the nonevolving population to the XRB decreases rapidly with redshift, the fluctuations due to these sources are only weakly sensitive to the clustering evolution rate  $\epsilon$ . They are also little sensitive to the cutoff length of the 3D ACF at the angular separations relevant here. Therefore we now assign model ‘a’ (Fig. 3) to the *nonevolving* population (this model adequately describes the clustering properties of the general galaxy population at low redshift), and pursue our investigation by varying the *evolving* population parameters only.

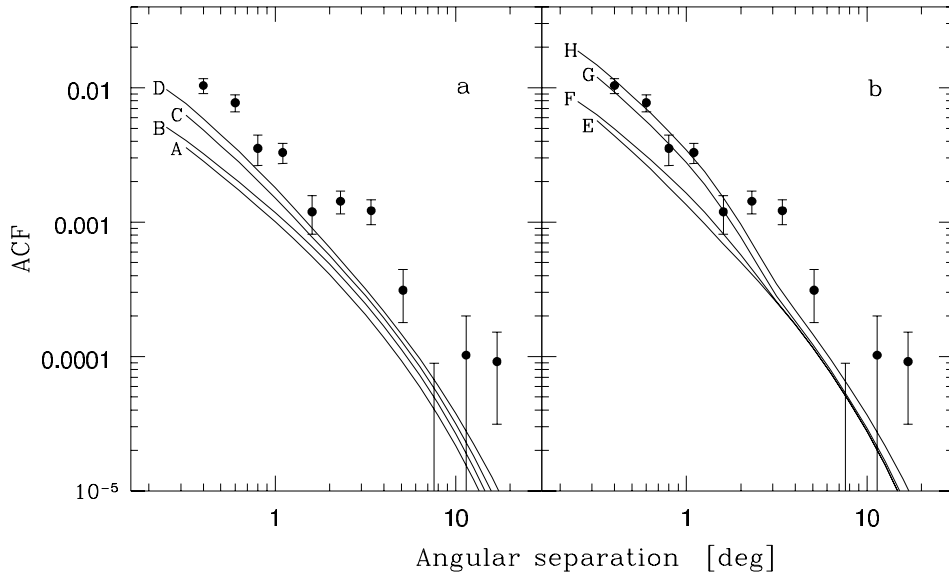


**Fig. 4a and b.** Autocorrelation functions of the RASS (dots) with error bars, and of selected models (curves); models with moderate clustering evolution - left panel, models with strong clustering evolution - right panel (see text for details).

Models with positive values of  $\epsilon$  (models A and B) fall short of the observed signal (Fig. 4a). In both these models, all the XRB sources are clustered like normal galaxies, and the amplitude of the spatial fluctuations increases linearly with redshift. Since models A and B only differ in their assumptions regarding the evolution of the X-ray light density, and since the two light density evolution models considered here (LD from Boyle et al. 1994 and LDDE from Miyaji et al. 1998b) are quite similar (Fig. 2), both models A and B generate similar 2D ACF, a factor of 2–3 below the observed signal in both cases.

Models C and D (Fig. 4a) assume a strong clustering amplitude (curve c in Fig. 3) stable in comoving coordinates ( $\epsilon = -1.2$ ). Although the discrepancy between these two models and the observations is globally reduced, it is still significant at separations smaller than  $2^\circ$ . The models shown in Fig. 4b assume strong clustering evolution with  $\epsilon = -2.5$ . In model E, the 3D ACF evolves according to Eq. 19 (‘vertical’ shift), as in models A thru D, while in models F, G and H the correlation functions evolves according to Eq. 20 (‘horizontal’ shift), which improves the fit at small separations. We conclude from this investigation that the observed angular correlation signal of the XRB seems to require a highly clustered population of sources, with more power on large scales than assumed here (due to the ‘cutoff length’) as well as stronger evolution than generally considered.

## 5. Discussions

Despite the large uncertainties in the ACF estimates and the relatively narrow range of angular separations available in the present analysis, we can draw general conclusions regarding the clustering properties of XRB sources. Fig. 4b shows that, if the XRB fluctuations are indeed produced by discrete sources distributed over a large range of redshift as observations suggest, then these sources must be strongly clustered and increasingly so at high redshift. However, using an observationally ‘reasonable’ range of parameters to describe known X-ray source populations, we are not able to reproduce the observed signal between

$2^\circ$  and  $5^\circ$ .<sup>2</sup> In principle, this discrepancy could be resolved by using still higher rates of clustering evolution and by radically increasing the 3D ACF amplitude at large separations. Alternatively, the strong signal between  $2^\circ$  and  $5^\circ$  could result from other effects than the clustering of X-ray sources distributed at cosmological distances.

One possible explanation is related to the Local Supercluster (LS). The equatorial plane of the LS crosses the area of sky used for our investigation. Of the 54 small galaxy groups members of the LS, 21–22 groups lie in the field we have used to measure the ACF (de Vaucouleurs 1975). They roughly cover  $1/10$  to  $1/5$  of the area under consideration. To produce an ACF signal of  $\sim 0.001$  at  $\theta \lesssim 5^\circ$ , the mean X-ray flux enhancement produced by these groups and averaged over the area of a typical group, should amount to  $0.07\text{--}0.1 \times$  the average XRB intensity. The observed flux produced by a single group would have to be of the order of  $(1 - 2) \times 10^{-11} \text{ erg s}^{-1} \text{ cm}^{-2}$  (0.5–2.0 keV) over the typical extent of a group in the LS, say, 25 sq. deg. The luminosity of such group, assuming a distance of 12 Mpc, would be  $\sim 3 \times 10^{41} \text{ erg s}^{-1}$ . This is only slightly above the luminosity expected from small groups of spiral galaxies, considering a typical luminosity of a few  $\times 10^{40} \text{ erg s}^{-1}$  per galaxy (e.g. Ehle et al. 1998). Using the X-ray data on nearby galaxies in the Fabbiano et al. (1992) catalogue, we find that the luminosities of these local groups are in the range  $5 \times 10^{40} - 2 \times 10^{41}$ , again slightly below the value required by the XRB fluctuations. Thus, it seems that the relatively large amplitude of the ACF at separations  $2^\circ - 5^\circ$  cannot be fully accounted for by local groups of galaxies, although the contribution of these objects to the XRB fluctuations is non negligible.

Despite our elaborate procedure to remove the contribution from the galactic emission, there are still some uncertainties on the residual galactic component. Our procedure performed

<sup>2</sup> The possible discrepancies between the models and the observations at larger separations are statistically insignificant (they do not exceed  $2\sigma$ ).

in S96 obtained  $\overline{n_g^h} \sim 3\%$  (Sect. 2.1). On the other hand, a simultaneous ASCA-ROSAT fit to the XRB with an extragalactic broken power-law component (with the power-law steepens at  $E \lesssim 1$  [keV]), hard-thermal component (Galactic halo), and a soft thermal component (local bubble) predicts  $\overline{n_g^h} \sim 7$ –10% for the sum of the two thermal components (Miyaji et al. 1998a). However, the spectral fit depends on a specific form of the broken power-law extragalactic component and the current quality of the spectra is not good enough to separate galactic and extragalactic component with good enough statistical precision for our purpose. While the separation procedure in S96 is the most reasonable way to remove the *fluctuation* from the galactic component based on our current knowledge, the underlying assumption of S96 that the galactic structure has a uniform spectrum is not assured. This may cause some residual fluctuation from our Galaxy.

Although the *ROSAT* data have allowed us to probe into the large scale distribution of high redshift sources, data with a higher signal-to-noise ratio and free from the galactic component are required to draw more definite conclusions. One way to reduce the uncertainties in the ACF measurement is to use a much larger area of sky. In the present analysis we were constrained to a solid angle of  $\sim 1$  steradian because of the apparent foreground contamination by hot gas within the Galaxy outside of this limited area. An all-sky survey at energies above 4 keV providing photon counts per unit area comparable to the RASS, would allow us to exploit areas 3–4 times larger in both galactic hemispheres free from the galactic contamination. In this respect, future missions similar to *ABRIXAS* would be of great importance.

### Appendix A: ACF from the *ROSAT* pointing observations

The full field of view of the *ROSAT* X-ray telescope/PSPC combination has radius of 57'. Soltan & Hasinger (1994) used only the central circular region of 30' diameter contained within the PSPC window support structure. They calculated the XRB ACF as the weighted average of independent ACF measurements in 46 such fields. This procedure is sensitive to the fluctuations on scales smaller than the field of view but effectively removes information on the nonuniform distribution of the X-ray flux on larger scales. The average count rates in these fields exhibit a large scatter, due to intrinsic XRB fluctuations on scales comparable to and larger than the field of view, and to fluctuations in the amount of particle contamination contributing to the total counts. Lack of information on the large scale fluctuations of the XRB did not allow for a comprehensive analysis of this question in the Soltan & Hasinger paper. The present results based on the *ROSAT* All-Sky Survey (RASS) indicate that the extragalactic XRB fluctuations in fact produce a significant scatter in the average background level of the separate pointings. When this effect is taken into account, the discrepancy between the ACF estimates based on pointings and on the RASS are effectively removed.

Let us assume that the *true* ACF at separations smaller than  $0:3$  is given by:  $w(\theta) = (\theta/\theta_0)^{-\gamma}$ , with  $\gamma \approx 0.8$ . Using the

RASS ACF estimate of  $w(0:3) \approx 1.3 \times 10^{-2}$ , we get  $\theta_0 \approx 1.3 \times 10^{-3}$ . The second moment of the total photon counts in the *ROSAT* pointing is (Peebles 1980):

$$\mu_2 = N + \left(\frac{N}{\Omega}\right)^2 \int_{\Omega} d\omega_1 d\omega_2 w(\theta_{12}), \quad (\text{A1})$$

where  $N$  denotes the average counts in a field of view of solid angle  $\Omega$  and  $\theta_{12}$  is the angular separation between  $d\omega_1$  and  $d\omega_2$ . With the above numerical values, we get:

$$\sigma = (\mu_2)^{1/2} \approx (N + 1.1 \times 10^{-2} N^2)^{1/2}. \quad (\text{A2})$$

The average number of counts per pointing used by Soltan & Hasinger is  $N = 1250$ . Thus the rms scatter in the average counts due to source clustering ( $\sigma/N$ ) is of order 0.1, exceeding the Poissonian fluctuations ( $N^{-1/2}$ ) by a factor of  $\sim 3.7$ .

The difference between the ACF determined using individual pointings and the ‘true’ ACF can be estimated as follows. Let  $W_i$  denote the ACF calculated from the  $i$ -th pointing:

$$W_i = \frac{(I_{i,m} - \overline{I}_i)(I_{i,n} - \overline{I}_i)}{\overline{I}_i^2}, \quad (\text{A3})$$

where  $I_{i,m}$  and  $I_{i,n}$  are the counts in the  $m$ -th and  $n$ -th pixels respectively, and the overlines denote the average over the  $i$ -th field of view. The average counts  $\overline{I}_i$  differ from field to field with the characteristic scatter defined in Eq. A2. To estimate the true ACF, we must calculate the ensemble average of the ACFs in the individual fields:

$$W = \left\langle \left(\frac{N_i}{N}\right)^2 W_i \right\rangle + \left(\frac{\sigma}{N}\right)^2, \quad (\text{A4})$$

where  $N_i$  are the counts in the  $i$ -th field, and  $\langle \dots \rangle$  define the average over a large number of pointings. The pointing analysis doesn’t show any correlation between  $W_i$  and  $N_i$  and therefore we can write:

$$W \approx \langle W_i \rangle + \left(\frac{\sigma}{N}\right)^2. \quad (\text{A5})$$

This shows that the ACF estimated from individual pointings was likely to be underestimated by  $\sim 0.01$ . Accounting for this statistical upward correction, the pointing estimate and the RASS estimate extrapolated to small separations become compatible.

*Acknowledgements.* The *ROSAT* project has been supported by the Bundesministerium für Bildung, Wissenschaft, Forschung und Technologie (BMBF/DARA) and by the Max-Planck-Society. AMS is grateful to Prof. G. Hasinger for his hospitality and financial support. This work has been partially supported by the Polish KBN grants 2 P03D 005 10 and 2 P03D 002 14.

### References

- Andreami P., Cristiani S., 1992, ApJ 398, L13
- Bagla J.S., 1998, MNRAS 299, 417
- Barcons X., Fabian A.C., Carrera F.J., 1998, MNRAS 293, 60

- Boughn S.P., 1998, *ApJ* 499, 533
- Boyle B.J., Shanks T., Georgantopoulos I., Stewart G.C., Griffiths R.E., 1994, *MNRAS* 271, 639
- Carrera F.J., Fabian A.C., Barcons X., 1997, *MNRAS* 285, 820
- Carrera F.J., Barcons X., Fabian A.C., et al., 1998, *MNRAS* 299, 229
- Connolly A.J., Szalay A.S., Brunner R.J., 1998, *ApJ* 499, L125
- Cress M.C., Helfand D.J., Becker R.H., Gregg M.D., White R.I., 1996, *ApJ* 473, 7
- Croom S.M., Shanks T., 1996, *MNRAS* 281, 893
- de Vaucouleurs G., 1975, *Nearby Groups of Galaxies*. In: Sandage A., Sandage M., Kristian K. (eds.) *Galaxies and the Universe. Stars and Stellar Systems Vol. IX*, The University of Chicago Press, Chicago & London, p. 557
- Ehle M., Pietsch W., Beck R., Klein U., 1998, *A&A* 329, 39
- Fabbiano G., Kim D.-W., Trinchieri G., 1992, *ApJS* 80, 531
- Georgantopoulos I., Shanks T., 1994, *MNRAS* 271, 773
- Groth E.J., Peebles P.J.E., 1977, *ApJ* 217, 385
- Hasinger G., 1992, *ROSAT Deep Surveys*. In: Brinkmann W., Trümper J. (eds.) *Proc. MPE Conf., X-ray Emission from Active Galactic Nuclei and the Cosmic X-ray Background*. MPE, Garching
- Hasinger G., 1998, *Astron. Nachr.* 319, 37
- Hasinger G., Burg R., Giacconi R., et al., 1998, *A&A* 329, 482
- La Franca F., Andreani P., Cristiani S., 1998, *ApJ* 497, 529
- Limber D.N., 1953, *ApJ* 117, 134
- Matarrese S., Coles P., Lucchin F., Moscardini L., 1997, *MNRAS* 286, 115
- Miyaji T., Ishisaki Y., Ogasaka Y., et al., 1998a, *A&A* 334, L13
- Miyaji T., Hasinger G., Schmidt M., 1998b, *Highlights in X-ray Astronomy*. In Honour of Joachim Trümper's 65th Birthday, astro-ph/9809398
- Moscardini L., Coles P., Lucchin F., Matarrese S., 1998, *MNRAS* 299, 95
- Peacock J.A., 1998, astro-ph/9805208
- Peebles P.J.E., 1980, *The Large-Scale Structure of the Universe*. Princeton University Press, Princeton, New Jersey
- Plucinsky P.P., Snowden S.L., Briel U.G., Hasinger G., Pfeiffermann E., 1993, *ApJ* 418, 519
- Ratcliffe A., Shanks T., Parker Q.A., Fong R., 1998, *MNRAS* 296, 191
- Roche N., Eales S.A., 1998, astro-ph/9803331
- Schmidt M., Hasinger G., Gunn J., et al., 1998, *A&A* 329, 495
- Shanks T., Boyle B.J., 1994, *MNRAS* 271, 753
- Shepherd C.W., Carlberg R.G., Yee H.K.C., Ellingson E., 1997, *ApJ* 479, 82
- Snowden S.L., Freyberg M.J., 1993, *ApJ* 404, 403
- Snowden S.L., Plucinsky P.P., Briel U.G., Hasinger G., Pfeiffermann E., 1992, *ApJ* 393, 819
- Snowden S.L., McCammon D., Burrows D., Mendenhall J.A., 1994, *ApJ* 424, 714
- Snowden S.L., Freyberg M.J., Plucinsky P.P., et al., 1995, *ApJ* 454, 643
- Snowden S.L., Egger R., Freyberg M.J., et al., 1997, *ApJ* 485, 125
- Soltan A., Hasinger G., 1994, *A&A* 288, 77
- Soltan A.M., Hasinger G., Egger R., Snowden S., Trümper J., 1996, *A&A* 305, 17 (S96)
- Soltan A.M., Hasinger G., Egger R., Snowden S., Trümper J., 1997, *A&A* 320, 705
- Tegmark M., Peebles P.J.E., 1998, *ApJ* 500, L79
- Treyer M.A., Lahav O., 1996, *MNRAS* 280, 469
- Treyer M., Scharf C., Lahav O., et al., 1998, *Large Scale Fluctuations in the X-Ray Background*. In: Mueller V., Gottloeber S., Muecket J.P., Wambsgans J. (eds.) *Proceedings of the 12th Potsdam Cosmology Workshop*, World Scientific, p. 361
- Woods D., Fahlman G.G., 1997, *ApJ* 490, 11